The Astronomical Journal, 127:3102–3114, 2004 June

WEAK LENSING FROM SPACE. III. COSMOLOGICAL PARAMETERS

Alexandre Refregier,[1,2,3] Richard Massey,[2] Jason Rhodes,[3,4,5] Richard Ellis,[3] Justin Albert,[3]
David Bacon,[6] Gary Bernstein,[7] Tim McKay,[8] and Saul Perlmutter[9]

Received 2003 May 27; accepted 2004 March 3

ABSTRACT

Weak gravitational lensing provides a unique method to directly map the dark matter in the universe and measure cosmological parameters. Current weak-lensing surveys are limited by the atmospheric seeing from the ground and by the small fields of view of existing space telescopes. We study how a future wide-field space telescope can measure the lensing power spectrum and skewness and thus set constraints on cosmological parameters. The lensing sensitivity was calculated using detailed image simulations and instrumental specifications studied in earlier papers in this series. For instance, the planned *SuperNova/Acceleration Probe* (*SNAP*) mission will be able to measure the matter density parameter Ω_m and the dark energy equation-of-state parameter w with precisions comparable and nearly orthogonal to those derived with *SNAP* from supernovae. The constraints degrade by a factor of about 2 if redshift tomography is not used but are little affected if only the skewness is dropped. We also study how the constraints on these parameters depend on the survey geometry and define an optimal observing strategy.

Key words: cosmological parameters — gravitational lensing — large-scale structure of universe

1. INTRODUCTION

Weak gravitational lensing provides a unique method to directly map the distribution of mass in the universe (for reviews, see Bartelmann & Schneider 2001; Mellier et al. 2002; Hoekstra, Yee, & Gladders 2002; Refregier 2003). The coherent distortions that lensing induces on the shape of background galaxies have now been firmly measured from the ground and from space. The amplitude and angular dependence of this "cosmic shear" signal can be used to set strong constraints on cosmological parameters. Several surveys are now in progress to map larger areas and thus reduce the uncertainties in these parameters. However, future ground-based surveys will eventually be limited by the systematics induced by atmospheric seeing. Space-based observations do not suffer from this effect, but their statistics are currently limited by the small fields of view of existing space telescopes.

In this series of papers, we study how these limitations can be circumvented with wide-field imaging from space, using the planned *SuperNova/Acceleration Probe* (*SNAP*) mission[10] as a concrete example. In the first paper in this series (Rhodes et al. 2004, hereafter Paper I), we studied the instrumental characteristics and survey strategy for such a mission, showing that it would provide both excellent statistics and reduced systematics relevant to weak lensing. In a subsequent paper (Massey et al. 2004, hereafter Paper II), we used detailed image simulations to compute the sensitivity for measuring weak lensing shear from space and, thus, to derive high-resolution maps of the dark matter in the local universe.

In this paper, we use the previously derived lensing sensitivity (see Papers I and II) to determine the constraints that can be placed on cosmological parameters by means of weak lensing from space. We consider quintessence (QCDM) models with a dark energy component with arbitrary constant equation-of-state parameter w. We compute the lensing power spectrum and skewness and their associated errors for different survey strategies. We study how the photometric redshifts derived from the *SNAP* filter set can be used to study the evolution of the lensing power spectrum. We then compare the resulting lensing constraints on cosmological parameters with those derived from supernovae. Earlier studies of the constraints on dark energy from generic weak-lensing surveys can be found in Hui (1999), Benabed & Bernardeau (2001), Hu (2002), Huterer (2002), Weinberg & Kamionkowski (2003), and Munshi & Wang (2003). While these authors have considered generic weak-lensing surveys, we use realistic redshift distributions, lensing sensitivities, and photometric redshift errors relevant to the concrete case of *SNAP*. This allows us to include the effects of photometric redshift errors and leakage between redshift bins, and to study the trade-off between width and depth in future surveys. We also study how the measurement of the skewness can be combined with power spectrum tomography to improve the accuracy of the determination of cosmological parameters.

This paper is organized as follows: In § 2, we summarize the characteristics of the *SNAP* mission. In § 3, we describe its capabilities for deriving photometric redshifts. In § 4, we describe the cosmological models we will consider. In § 5, we compute the lensing power spectrum, its associated errors, and its redshift evolution. In § 6, we compute the skewness of the

---

[1] Service d'Astrophysique, CEA Saclay, F-91191 Gif-sur-Yvette, France; refregier@cea.fr.

[2] Institute of Astronomy, Madingley Road, Cambridge CB3 0HA, UK.

[3] Department of Astronomy, 105-24, California Institute of Technology, 1201 East California Boulevardd, Pasadena, CA 91125.

[4] Laboratory for Astronomy and Solar Physics, Code 681, NASA Goddard Space Flight Center, Greenbelt, MD 20771.

[5] NASA/NRC Research Associate.

[6] Institute for Astronomy, University of Edinburgh, Blackford Hill, Edinburgh EH9 3HJ, UK.

[7] Department of Physics and Astronomy, University of Pennsylvania, 209 South 33rd Street, Philadelphia, PA 19104.

[8] Department of Astronomy, 830 Dennison Building, University of Michigan, Ann Arbor, MI 48109.

[9] Lawrence Berkeley National Laboratory, 1 Cyclotron Road, Berkeley, CA 94720.

[10] See http://snap.lbl.gov.

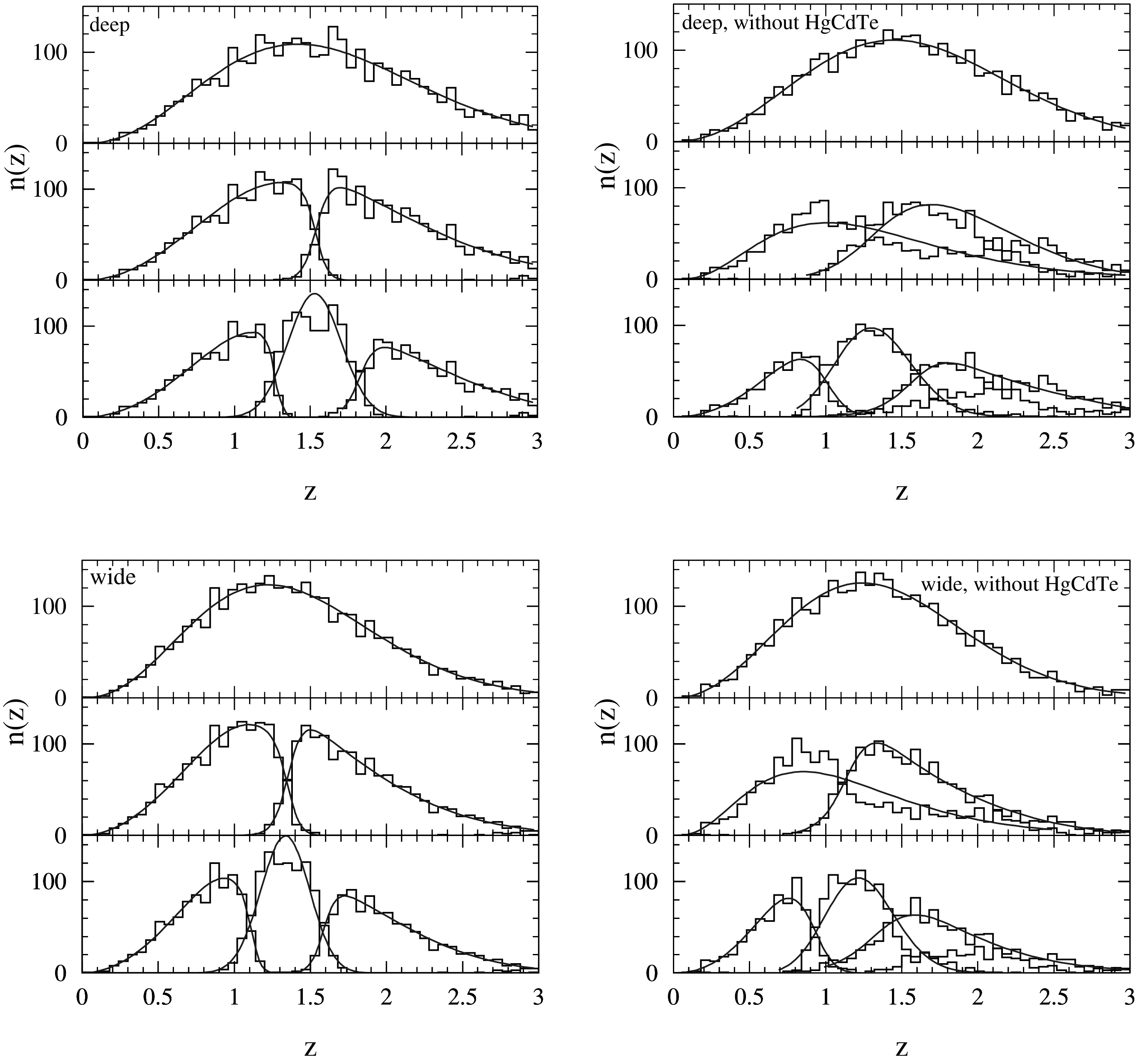

FIG. 1.—Redshift bins derived from photometric redshifts. In each of the four panels, the histograms show the redshift distributions resulting from cuts in photometric redshifts aimed at producing one, two, and three redshift bins from top to bottom, respectively. The solid curves correspond to fits for the analytical form of eqs. (1)–(2). The top and bottom panels correspond to the deep and wide *SNAP* surveys, respectively. In the left panels, the full set of nine optical and near-IR (HgCdTe) *SNAP* filters were used to estimate the photometric redshifts. In the right panels, only the six optical filters were used. In all cases, the normalization is arbitrary.

shear field and associated errors. In § 7, we compute the constraints that can be set on cosmological parameters from measurements of the power spectrum and skewness. Our conclusions are summarized in § 8.

2. THE *SNAP* MISSION

The *SNAP* satellite will consist of a 2 m telescope in space with a field of view of 0.7 deg^2 (see the *SNAP* Web site and also Paper I). The mission lifetime will be divided between two deep 16 month surveys and a 5 month wide survey. The deep surveys will cover 15 deg^2 and are primarily designed to search for Type Ia supernovae. They will also be invaluable for mapping the dark matter by means of weak lensing (see Paper II). The wide survey is designed primarily for weak lensing and will cover 300 deg^2. The spacecraft will be in a high elliptical orbit with good thermal stability, thus affording stable image quality and a low level of systematics. Details of the performance of the instrument for weak lensing and of the survey strategy can be found in Paper I.

3. PHOTOMETRIC REDSHIFTS

The *SNAP* focal plane will be partially covered by CCDs sensitive to nine optical and near-IR bands. Paper II describes how this filter set affords excellent photometric redshifts. This was tested using the ‘‘hyperz’’ code (Bolzonella, Miralles, &

TABLE 1

Survey Parameters and Redshift Distributions

Survey	z Bins	$t_{\rm exp}$[a] (s)	$t_{\rm tot}$ (months)	A (deg^2)	n_g (arcmin^{-2})	σ_γ[b]	z_m	z_0	α	β	z_+	ζ_+	z_-	ζ_-
Deep	...	20000	32	15	260	0.36	1.43	1.31	2.00	2.00	...	...	...	...
Wide	...	2000	5	300	100	0.31	1.23	1.13	2.00	2.00	...	...	...	...
	1/2	2000	5	300	50	0.31	0.96	1.32	1.94	3.38	1.36	0.042	...	...
	2/2	2000	5	300	50	0.31	1.73	1.51	0.53	2.16	...	...	1.36	0.048
	1/3	2000	5	300	33	0.31	0.81	1.13	1.95	5.55	1.11	0.031	...	...
	2/3	2000	5	300	33	0.31	1.31	0.80	20.07	3.45	1.11	1.515	1.59	1.515
	3/3	2000	5	300	33	0.31	1.93	1.57	1.50	2.48	...	...	1.59	0.042
Wide+	...	1000	5	600	68	0.30	1.17	1.07	2.00	2.00	...	...	...	...
Wide−	...	4000	5	150	150	0.33	1.31	1.20	2.00	2.00	...	...	...	...

Note.—The redshift-bin distributions assume the use of the nine *SNAP* filters, including the near-IR detectors.

[a] Exposure time in each optical filter, equal to half the exposure time for the near-IR filters.

[b] The rms shear $\sigma_\gamma = \langle|\gamma|^2\rangle^{1/2}$ from noise and intrinsic ellipticity.

Pelló 2000) to generate simulated galaxy spectra and recovered photometric redshifts. Using all nine filters, we found that redshifts can be recovered with a 1 σ precision better than 0.03. Including the near-IR detectors prevents catastrophic failures in redshift estimation by eliminating strong degeneracies between low ($z \lesssim 0.5$) and high ($z \gtrsim 1$) redshift bins (seePaper II).

These high-precision photometric redshifts will allow us to construct three-dimensional maps of the dark matter (see Paper II). They will also be useful in studying the evolution of

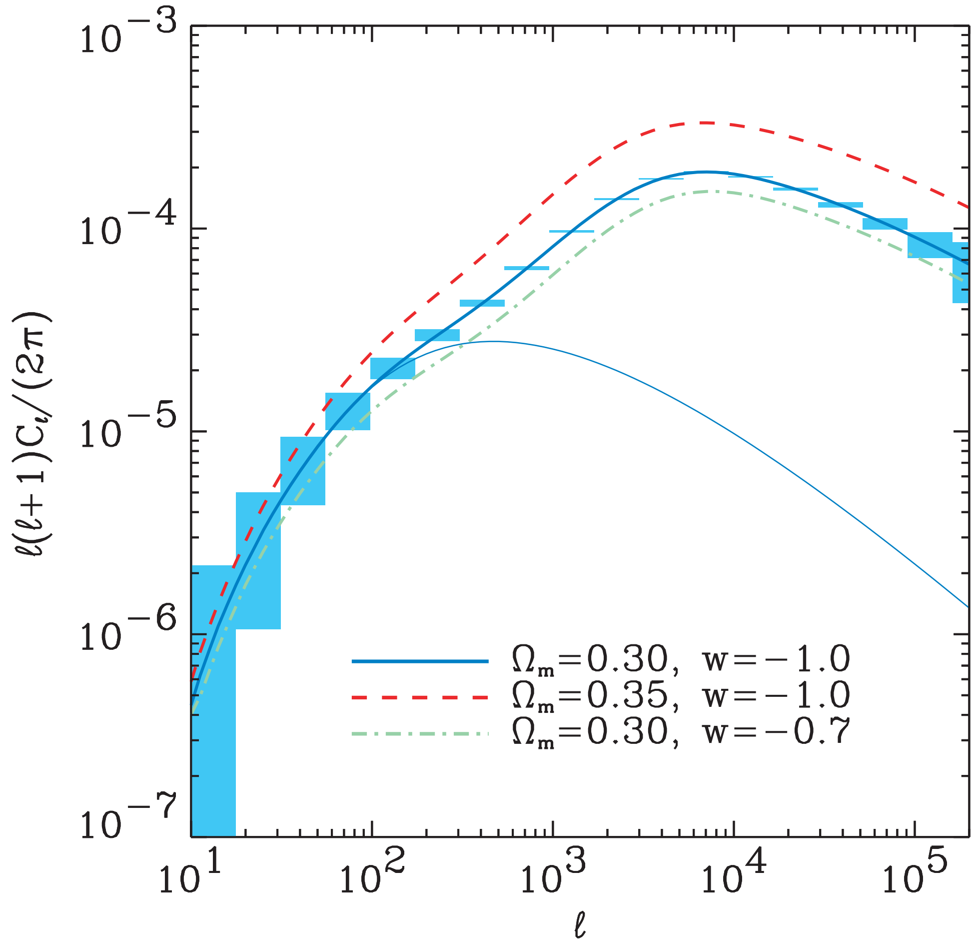

Fig. 2.—Weak-lensing power spectrum for several cosmological models. The top solid line shows the weak-lensing power spectrum C_l for the fiducial ΛCDM model with $\Omega_m = 0.30$ and $w = -1$. The bottom solid line shows the linear power spectrum for the same model. The dashed and dot-dashed lines show the nonlinear power spectra for variations of the model with $\Omega_m = 0.35$ and $w = -0.7$, respectively. In all cases, $\Omega_q = 1 - \Omega_m$, $h = 0.7$, $\Omega_b = 0.047$, $n = 1$, and *COBE* normalization were assumed. The redshift distribution was taken to be that for the *SNAP* wide survey (unbinned) with a median redshift of $z_m = 1.23$. The boxes correspond to the band-averaged 1 σ errors about the fiducial model for the *SNAP* wide survey (300 deg^2 area, 100 galaxies arcmin^{-2}, and an intrinsic shear dispersion of $\sigma_\gamma = 0.31$).

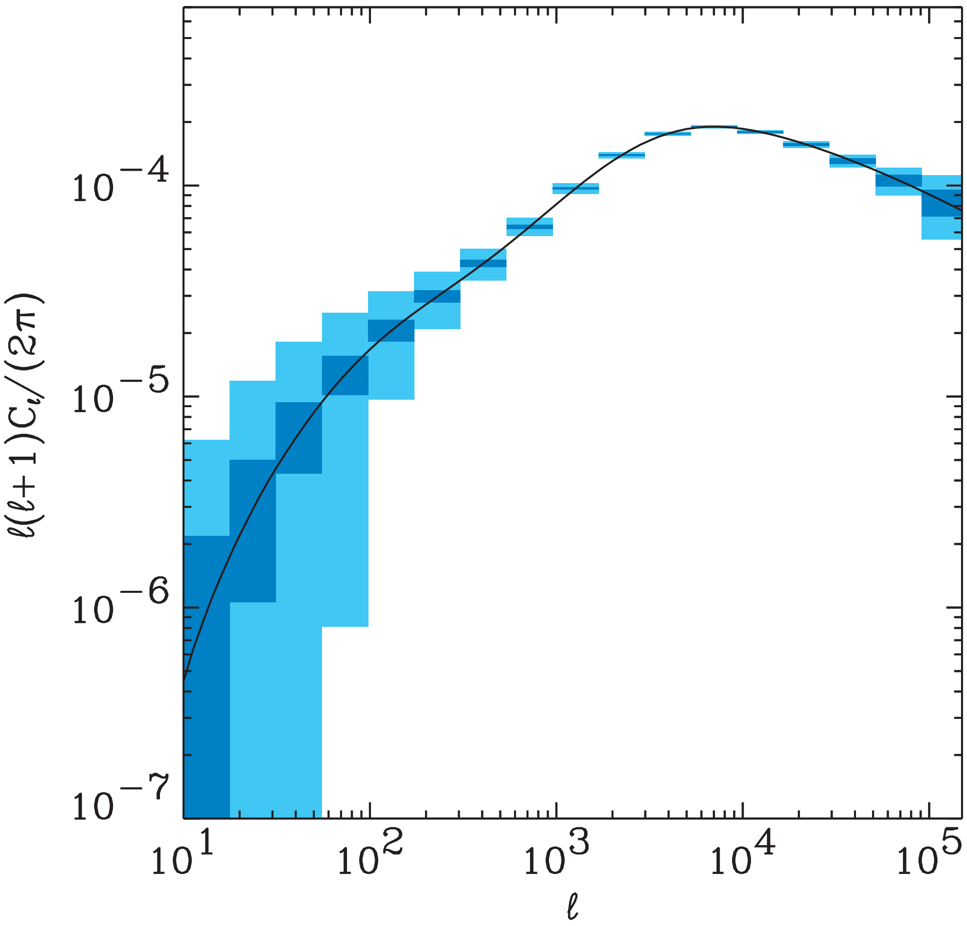

Fig. 3.—Measurement of the weak-lensing power spectrum with the wide and deep *SNAP* surveys. The solid line shows the power spectrum for the fiducial ΛCDM model of the previous figure. The light and dark boxes show the band-averaged 1 σ errors for the deep and wide surveys, respectively.

the lensing statistics. Figure 1 shows how photometric redshifts can be used to group galaxies into redshift bins. The input redshift distribution $n(z)$ was assumed to have the form

$$n(z) \propto z^{\alpha} e^{-(z/z_0)^{\beta}}, \qquad (1)$$

where z_0, α, and β are parameters estimated from existing deep redshift surveys (see Paper II). Table 1 lists the values of these parameters for the deep and wide surveys, along with the associated median redshift z_m, the surface density n_g of galaxies usable for lensing, and the survey solid angle A. The exposure time $t_{\rm exp}$ for each optical filter, along with the total observing time $t_{\rm tot}$ for the survey, is also listed. The figure shows the redshift distributions that result from binning the galaxies into two and three photometric redshift bins, with approximately the same number of galaxies in each bin. With the near-IR detectors (*left*), the photometric redshifts afford excellent separation between the bins. In the absence of these detectors (*right*), the separation between bins degrades, because of the increased noise and degeneracies in the photometric redshifts (see Fig. 6 in Paper II). In the following, we will always assume that the near-IR detectors are available.

The redshift distribution of each bin can be described analytically by multiplying the input redshift distribution $n(z)$ in equation (1) by the high-z and low-z filter functions $f_+(z)$ and/or $f_-(z)$, given by

$$f_{\pm}(z) = (1 + e^{\pm(z_{\pm} - z)/\zeta_{\pm}})^{-1}, \qquad (2)$$

where z_+ and z_- are the cutoff redshifts and ζ_+ and ζ_- are smearing factors arising from the finite photometric redshift accuracy. Fits to the redshift-bin distributions using these analytical forms are shown in Figure 1. The values of the resulting parameters for two and three redshift bins are listed in Table 1. In § 5.3, we study how multiple redshift bins can be used to measure the evolution of the lensing power spectrum and thus improve the accuracy of the measurement of cosmological parameters.

4. COSMOLOGICAL MODEL

We consider a cosmology with an expansion parameter $a = (1 + z)^{-1}$ that is determined by a matter component and a dark energy (or "quintessence") component with present-day density parameters Ω_m and Ω_q, respectively. The equation of state of the dark energy is parameterized by $w = p_q/\rho_q$, which we assume to be constant and is equal to -1 in the case of a cosmological constant. The evolution of the expansion parameter is given by the Hubble constant H through the Friedmann equation

$$H = \dot{a}/a = H_0(\Omega_m a^{-3} + \Omega_q a^{-3(1+w)} + \Omega_\kappa a^{-2})^{1/2}, \qquad (3)$$

where $\dot{a} = da/dt$ and the total and curvature density parameters are Ω and $\Omega_\kappa = 1 - \Omega$, respectively. The present value of the Hubble constant is parameterized as $H_0 = 100\,h$ km s^{-1} Mpc^{-1}.

As a reference model, we consider a fiducial cold dark matter model with a cosmological constant (ΛCDM) with

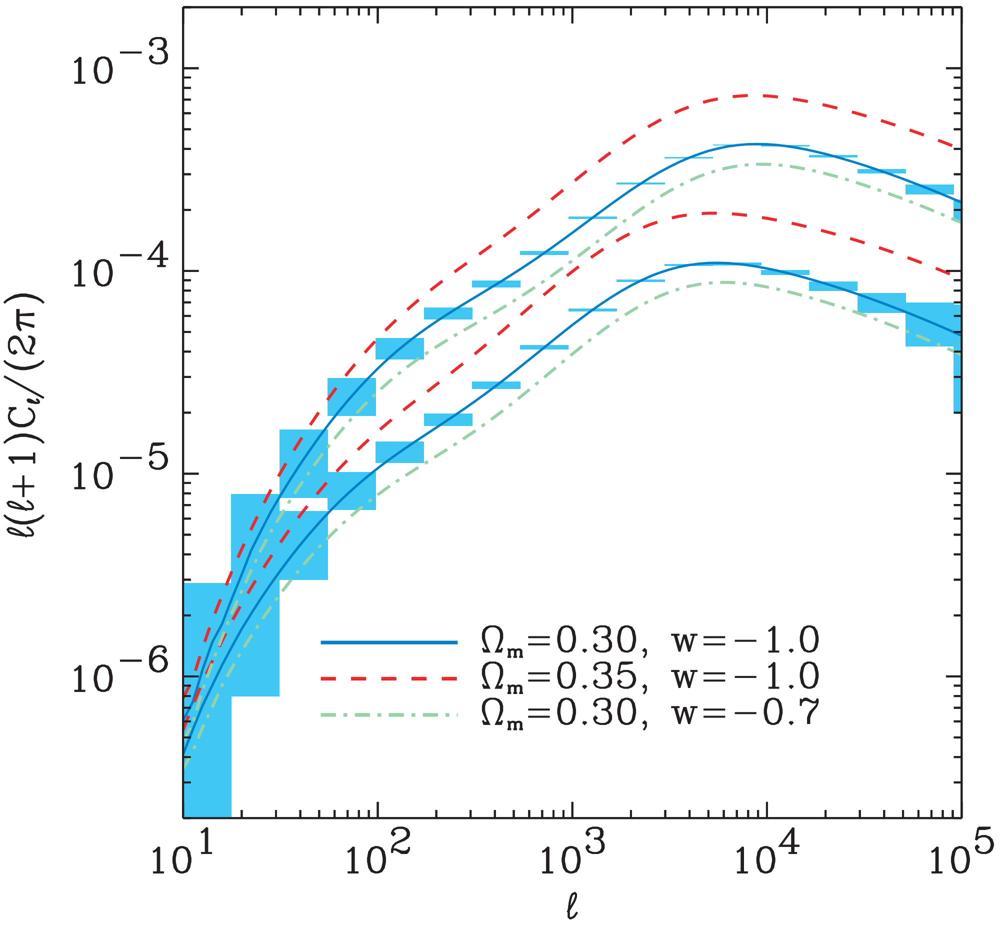

FIG. 4.—Redshift dependence of the lensing power spectrum. The solid lines and associated 1 σ error boxes show the lensing power spectrum for the two redshift bins of the *SNAP* wide survey with median galaxy redshifts of $z_m = 0.96$ (*bottom line*) and 1.73 (*top line*). As in Fig. 2, the dashed and dot-dashed lines correspond to perturbations about the fiducial model (*solid line*) for each redshift bin.

parameters $\Omega_m = 0.30$, $\Omega_b = 0.047$, $n = 1$, $h = 0.7$, and $w = -1$, consistent with the recent *WMAP* experiment (see Tables 1 and 2 in Spergel et al. 2003). In agreement with this experiment, we assume that the universe is flat, that is, $\Omega = \Omega_m + \Omega_q = 1$. (Note that in our notation, Ω_m includes both dark matter and baryons.) The shape parameter for the matter power spectrum is taken to be $\Gamma = \Omega_m h \exp\,(-\Omega_b[1 + (2h)^{1/2}/\Omega_m])$ as prescribed by Sugiyama (1995). The matter power spectrum is normalized according to the *COBE* normalization (Bunn & White 1996), which corresponds to $\sigma_8 = 0.88$. This is consistent with the *WMAP* results (Spergel et al. 2003) and with the average of recent cosmic shear measurements (see compilation tables in Mellier et al. 2002, Hoekstra et al. 2002, and Refregier 2003). In the following, we will consider deviations from this reference model.

5. WEAK-LENSING POWER SPECTRUM

5.1. *Theory*

The weak lensing power spectrum is given by

$$C_l = \frac{9}{16}\left(\frac{H_0}{c}\right)^4 \Omega_m^2 \int_0^{\chi_h} d\chi \left[\frac{g(\chi)}{ar(\chi)}\right]^2 P(l/r, \chi) \qquad (4)$$

(see, e.g., Bartelmann & Schneider 2001; Hu & Tegmark 1999; see Bacon, Refregier, & Ellis 2000 for conventions), where $r(\chi)$ is the comoving angular diameter distance and χ_h corresponds to the comoving radius to the horizon. The nonlinear matter power spectrum $P(k, z)$ is computed using the transfer function from Bardeen et al. (1986; with the conventions of Peacock 1997), thus ignoring the corrections on large scales for quintessence models (Ma et al. 1999). The growth factor and *COBE* normalization for arbitrary values of w were computed using the fitting formulae from Ma et al. (1999). Considerable uncertainties remain for the nonlinear corrections in quintessence models (see discussion in Huterer 2002). Here we use the fitting formula from Peacock & Dodds (1996) but acknowledge that it differs significantly from that given by Ma et al. (1999). The impact of this uncertainty is discussed below in § 8. The radial weight function g is given by

$$g(\chi) = 2\int_{\chi}^{\chi_h} d\chi'\, n(\chi')\frac{r(\chi)r(\chi' - \chi)}{r(\chi')}, \qquad (5)$$

where $n(\chi)$ is the probability of finding a galaxy at comoving distance χ and is normalized as $\int d\chi\, n(\chi) = 1$. For our purposes, we use the analytical fits for $n(z)$ given in equations (1)–(2) along with the parameter values listed in Table 1.

Figure 2 shows the lensing power spectrum for the fiducial ΛCDM model. Deviations from the model corresponding to variations in Ω_m and w are also shown. All models shown are *COBE* normalized. The linear power spectrum for the fiducial model is also shown, highlighting the importance of nonlinear evolution for $l \gtrsim 100$.

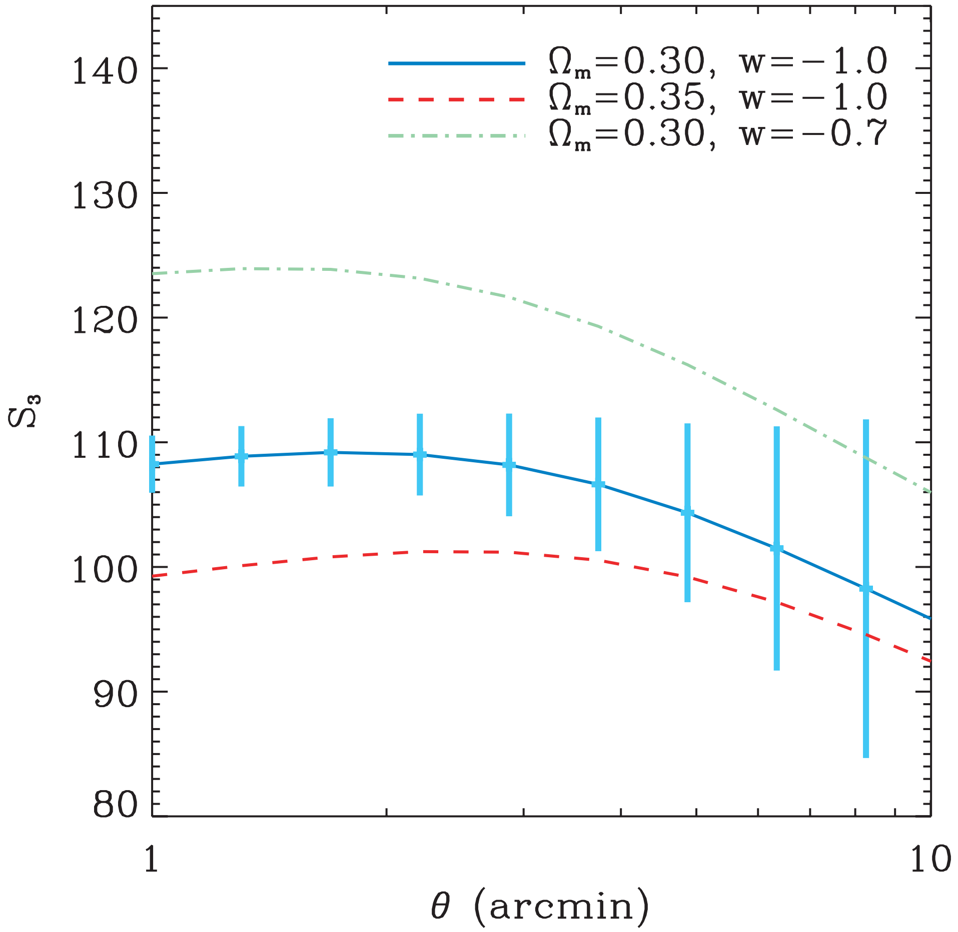

FIG. 5.—Skewness S_3 as a function of scale. The three cosmological models from Fig. 2 are displayed. The 1 σ error bars correspond to the *SNAP* wide survey.

5.2. *Measurement Uncertainties*

Neglecting non-Gaussian corrections, the rms uncertainty in measuring the lensing power spectrum C_l is given by

$$\Delta C_l = \sqrt{\frac{2}{(2l+1) f_{\rm sky}}}\left(C_l + \frac{\sigma_\gamma^2}{2n_g}\right) \qquad (6)$$

(Kaiser 1998; Hu & Tegmark 1999; Huterer 2002), where $f_{\rm sky}$ is the fraction of the sky covered by the survey, n_g is the surface density of usable galaxies, and $\sigma_\gamma^2 = \langle|\gamma|^2\rangle$ is the shear variance per galaxy arising from intrinsic shapes and measurement errors. Values of σ_γ for the different *SNAP* surveys were derived from the image simulations in Paper II and are listed in Table 1.

Figure 2 shows the resulting band-averaged errors for the fiducial ΛCDM model measured with the *SNAP* weak-lensing survey. The sensitivity afforded by this survey is excellent and will allow us to easily distinguish between the different cosmological models shown. Figure 3 compares the precision expected for the wide and deep *SNAP* surveys. The deep survey clearly yields lower precision for the measurement of the power spectrum, despite its longer observing time. It will however be ideally suited to produce high-resolution maps of the dark matter (see Paper II).

5.3. *Evolution of the Power Spectrum*

As discussed in § 3, the *SNAP* filter set will allow us to divide the galaxies into several redshift bins. Possible redshift-bin configurations are shown in Figure 1. The lensing power spectrum can then be measured separately in each bin, yielding a tomography of the mass distribution along the line of sight (Hu 1999; Taylor 2001; Hu & Keeton 2002).

Figure 4 shows, for instance, the lensing power spectrum and associated error bars for the two redshift bins derived from the *SNAP* wide survey with median redshifts $z_m \simeq 0.96$ and $z_m \simeq 1.73$ (see Fig. 1 and Table 1). Clearly, the amplitude of the power spectrum is much larger for the more distant bin. The sensitivity afforded by the *SNAP* wide survey will allow us to easily measure each power spectrum separately. In § 7.4 below, we show how the measurement of the lensing power spectrum at different redshifts improves the precision of cosmological parameters.

6. SKEWNESS

Nonlinear gravitational instability is known to produce non-Gaussian features in the cosmic shear field. The power spectrum therefore does not contain all the information available from weak lensing. We consider the most common measure of non-Gaussianity, namely, the skewness S_3, which is defined as

$$S_3(\theta) \equiv \langle\kappa^3\rangle/\langle\kappa^2\rangle^2 \qquad (7)$$

(see, e.g., Bernardeau, van Waerbeke, & Mellier 1997), where κ is the convergence, which can be derived from the shear field γ_i, and the brackets denote averages over circular top-hat

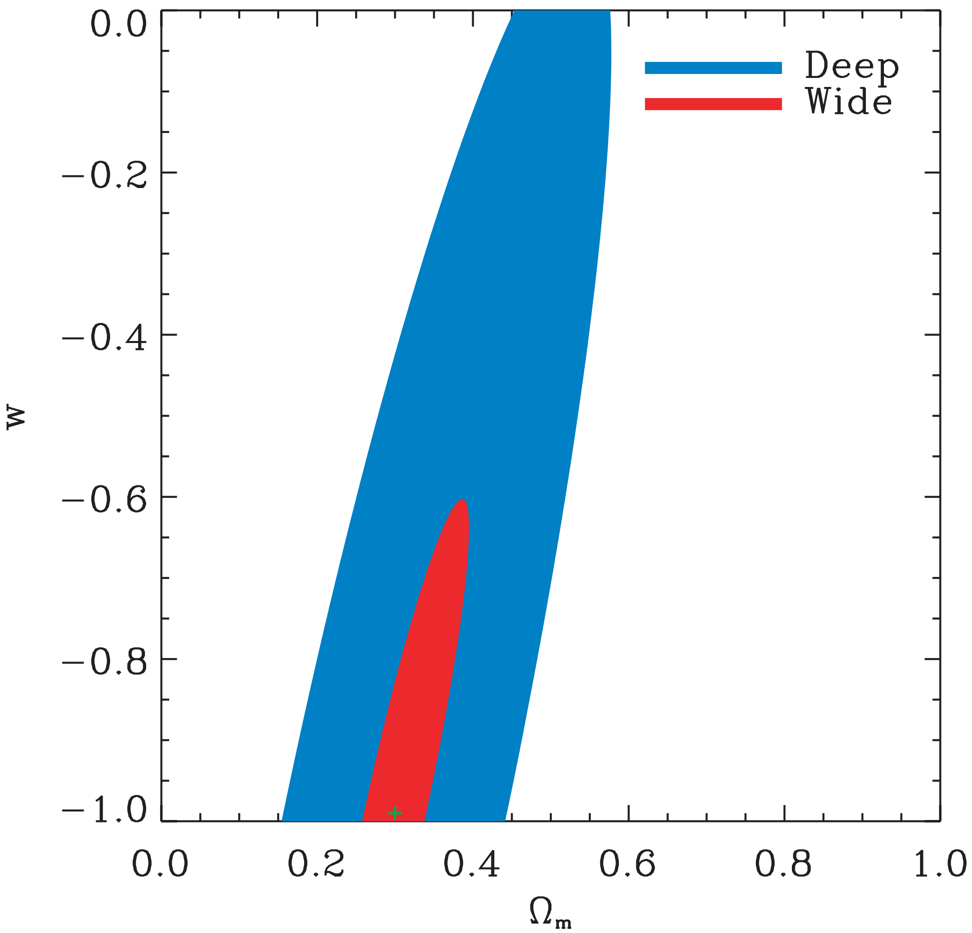

FIG. 6.—Constraints on Ω_m and w from the power spectrum derived from the wide and deep *SNAP* surveys. The contours correspond to the 68% confidence level and have been marginalized over h, n, and Ω_b, with a 7% rms *COBE* prior for the power spectrum normalization δ_h. The cosmological model was assumed to be flat ($\Omega_m + \Omega_q = 1$). The range of scales used for the power spectrum is $10 < l < 2 \times 10^5$.

cells of radius θ. The denominator is the square of the convergence variance, which is given by

$$\langle \kappa^2 \rangle = \langle \gamma^2 \rangle \simeq \frac{1}{2\pi} \int dl\, l C_l |W_l|^2, \qquad (8)$$

where $W_l \equiv 2J_1(l\theta)/(l\theta)$ is the window function for such cells and C_l is the lensing power spectrum given by equation (4).

To evaluate the numerator of equation (7), we use the approximation of Hui (1999), who used the "hyperextended perturbation theory" of Scoccimarro & Frieman (1999) and obtained

$$\langle \kappa^3 \rangle \simeq \frac{81\pi^2}{16} \left(\frac{H_0}{c} \right)^6 \Omega_m^3 \times \int_0^{\chi_h} d\chi\, \frac{g^3}{a^3 r^4} \left[\int d^2 l \sqrt{Q_3} P(l/r, \chi) |W_l|^2 \right]^2, \qquad (9)$$

where $Q_3 = (4-2^n)/(1+2^{n+1})$ and n is the linear power spectral index at scale $k = l/r$. While more accurate approximations for third-order statistics now exist (see van Waerbeke et al. 2001b and references therein), the present one suffices for our purpose.

Figure 5 shows the skewness as a function of scale for the same cosmological models considered in Figure 2. The skewness is only weakly dependent on the angular scale θ, but it depends more strongly on Ω_m and w.

The computation of the exact error for S_3 is challenging, as it depends on sixth-order terms, which are difficult to compute in the nonlinear regime. Instead, we compute the rms error for a Gaussian field (in which case $S_3 = 0$) and introduce a multiplicative factor $f_{\rm ng}$ to correct for non-Gaussianity of the convergence field and obtain

$$(\Delta S_3)^2 = \frac{15}{N_c} \frac{\left[f_{\rm ng}^{2/3} \langle \kappa^2 \rangle + \sigma_\kappa^2/(n_g A_c) \right]^3}{\langle \kappa^2 \rangle^2}, \qquad (10)$$

where $A_c = \pi\theta^2$ is the cell solid angle, $N_c = A/A_c$ is the number of cells, which are assumed to be independent, and A is the total solid angle of the survey. The rms dispersion of the convergence arising from the intrinsic dispersion of the galaxy ellipticities and from measurement noise is related to the associated rms shear by $\sigma_\kappa^2 = \sigma_\gamma^2$. The non-Gaussian correction factor only applies to the cosmic variance term (the first term), since the noise term can be assumed to be Gaussian. It is set to $f_{\rm ng} \simeq 2$, as estimated by White & Hu (2000), who compared Gaussian estimates with errors derived from (noise-free) numerical simulations.

The resulting errors for the *SNAP* wide survey are shown in Figure 5, for the fiducial ΛCDM model. The sensitivity

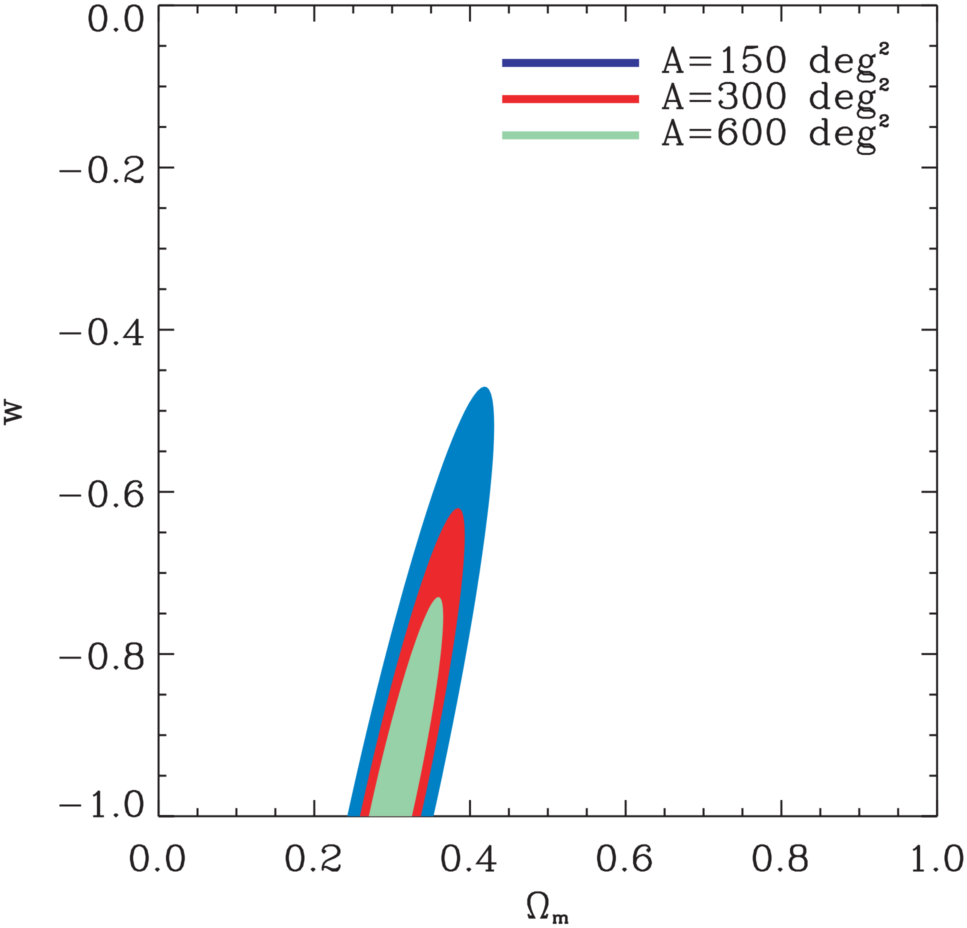

FIG. 7.—Dependence of the confidence contours on the survey area A, for a varying survey observing time $t_{\rm tot}$. The depth of the survey is fixed to that of the wide *SNAP* survey (300 deg^2, $t_{\rm tot} = 5$ months). Survey areas of 150 and 600 deg^2 would thus require an observing time of 2.5 and 10 months, respectively. The conventions and marginalizations are as described in the legend to Fig. 6.

afforded by this survey will allow us to easily distinguish between these models via the skewness.

7. CONSTRAINTS ON COSMOLOGICAL PARAMETERS

7.1. *Fisher Matrix*

The constraints that can be set on cosmological parameters can be estimated using the Fisher matrix

$$F_{ij} = -\left\langle \frac{\partial \ln \mathcal{L}}{\partial p_i \, \partial p_j} \right\rangle \tag{11}$$

(e.g., Hu & Tegmark 1999), where $\mathcal{L}$ is the likelihood function and p_i is a set of model parameters. The inverse $\mathbf{F}^{-1}$ provides a lower limit for the covariance matrix of the parameters.

For a measurement of the power spectrum, this reduces to

$$F_{ij} = \sum_l (\Delta C_l)^{-2} \frac{\partial C_l}{\partial p_i} \frac{\partial C_l}{\partial p_j}, \tag{12}$$

where the summation is over modes l that can be reliably measured. Note that this expression assumes that the errors are Gaussian and that the multipoles are not correlated. These effects have been shown to increase the errors on cosmological parameters by only about 15% (Cooray & Hu 2001) and have been neglected here.

Since the measurements of the skewness on different scales are strongly correlated, we conservatively consider only one scale, $\theta = 2'$, to compute the constraints from S_3. The associated Fisher matrix is then

$$F_{ij} = (\Delta S_3)^{-2} \frac{\partial^2 S_3}{\partial p_i \, \partial p_j}. \tag{13}$$

The joint constraints from the power spectrum combined with the skewness can be computed by adding the respective Fisher matrices.

7.2. *Baseline Surveys*

Figure 6 shows the joint constraints on w and Ω_m that can be derived from the wide and deep wide surveys. The contours correspond to the 68% confidence level and have been marginalized over h, n, and Ω_b. A *COBE* prior for the power spectrum normalization δ_h of 7% rms (Bunn & White 1997) was also assumed and marginalized over. The range of scales considered to evaluate the power spectrum is $10 < l < 2 \times 10^5$.

Clearly, the wide survey provides stronger constraints than the deep survey, even though its observing time is 6.4 times shorter. This follows from the fact that the increased surface density of resolved galaxies in the deep survey does not compensate for its smaller area. This can be seen by comparing

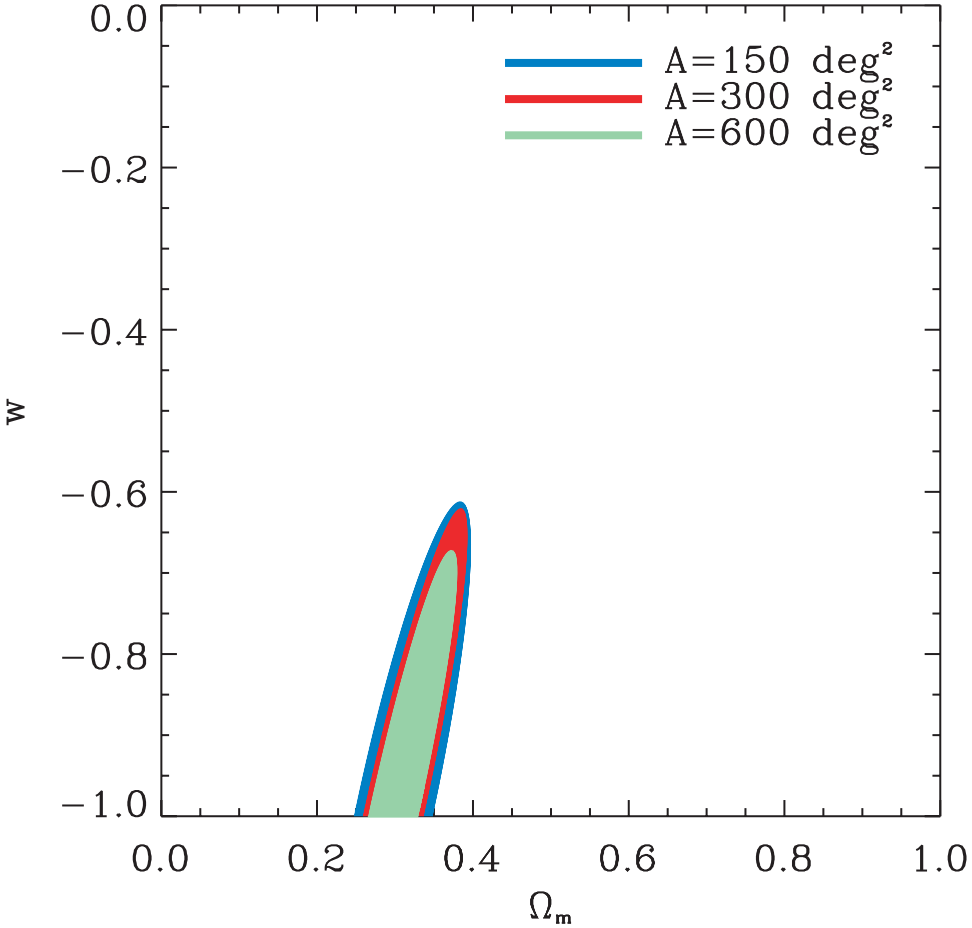

FIG. 8.—Dependence of the confidence contours on the survey area *A* for a fixed observing time of $t_{\rm tot}$ = 5 months. This corresponds to a trade-off between survey width and depth about the nominal *SNAP* wide survey (300 deg^2). The sensitivity to shear for each exposure time was derived from the image simulations described in Paper II.

the error bars for the power spectrum from each survey (see Fig. 3 and the discussion in § 5.2).

7.3. *Survey Strategy*

It is instructive to study the dependence of these constraints on the survey geometry. Figure 7 shows how the constraints on Ω_m and w change as the survey area A is halved or doubled while the depth of the survey is kept as that of the wide survey (see parameters for the wide survey in Table 1). As expected, the contours scale simply as $A^{-1/2}$ in this case.

More realistically, Figure 8 shows the same contours, but this time keeping the survey observing time constant at $t_{\rm tot}$ = 5 months, the allocated time for the wide survey. This amounts to a trade-off between area and depth for a fixed observing time. The survey parameters for each of the 150, 300, and 600 deg^2 cases are listed in Table 1, with entries “Wide−,” “Wide,” and “Wide+,” respectively. As can be seen in the figure, the constraints do not improve as fast as in the earlier case. Doubling the survey area from 300 to 600 deg^2, while reducing the depth correspondingly, leads to an improvement in the precision of w of only about 10%.

A wider and shallower survey is therefore preferred compared with the nominal wide survey, but it does not provide a substantial improvement. As explained in Paper I, the shallowness of the survey is limited by the finite telemetry bandwidth of the spacecraft and cannot be increased without performing lossy data compression or modification of the hardware. Moreover, a shallower survey will limit our ability to measure the redshift dependence of the lensing power spectrum (see § 5.3 and § 7.4 below). These considerations led to the choice of the baseline survey strategy of the *SNAP* wide survey (see Paper I).

7.4. *Tomography*

As discussed in § 5.3, the constraints can be improved by studying the redshift dependence of the lensing power spectrum. This can be done by subdividing the galaxy sample into several redshift bins using photometric redshifts.

Figure 9 shows how the constraints on w and Ω_m improve when the galaxies in the *SNAP* wide survey are split into two and three redshift bins. The redshift distribution $n(z)$ of each bin is that from the bottom left panel of Figure 1.

The parameters for these distributions are listed in Table 1. The constraints on both w and Ω_m improve by about a factor of 2 in precision when two bins are used instead of one. The gain from additional bins is not very significant. This results agrees with the conclusions of Huterer (2002) and Hu (2002), who considered more generic cases and simpler redshift distributions. Note that our analysis includes the effect of photometric redshift errors and of the resulting leakage from one bin to the other (see overlapping tails in Fig. 1).

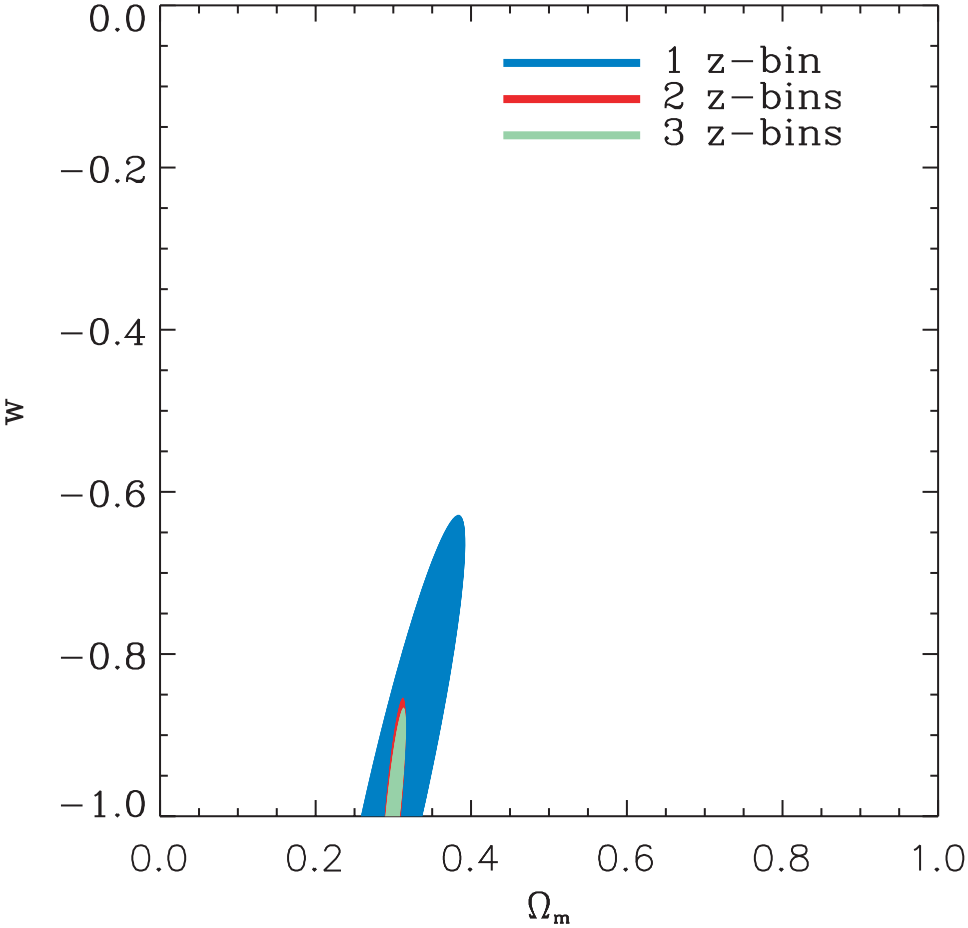

FIG. 9.—Improvement of the constraints on w and Ω_m from the use of tomography. One, two, and three redshift bins derived from photometric redshifts in the *SNAP* wide survey (with near-IR detectors) are displayed.

7.5. *Skewness*

As discussed in § 6, another way of improving the cosmological constraints is to also include a measurement of the skewness S_3. Figure 10 shows the contours on the Ω_m-w plane corresponding to the use of the power spectrum with and without tomography (with two redshift bins) and with and without skewness. As discussed in § 7.1, a measurement of S_3 at the single scale $\theta = 2'$ is conservatively considered. The addition of the skewness improves the precision of Ω_m by a little less than a factor of 2 but does not appreciably improve the precision of w. The former arises from the well-known fact that a measurement of S_3 helps to break the degeneracy between the power spectrum normalization and Ω_m (Bernardeau et al. 1997).

The improvements on both Ω_m and w from the inclusion of the skewness are however overwhelmed by the corresponding improvements derived from tomography. This shows that tomography is more powerful than the skewness to study dark energy, at least for conditions similar to those of the *SNAP* wide survey. Note that our treatment of the skewness using the Fisher matrix provides a lower limit for the parameter errors, since the error of the skewness is non-Gaussian (this is also true for the power spectrum). This conclusion will thus be a fortiori true for a full non-Gaussian treatment of the skewness error. The combined constraints using both tomography and skewness are also displayed in Figure 10.

7.6. *Comparison with Constraints from Supernovae*

The results described above show that weak lensing provides powerful constraints on dark energy, which can be compared with those derived with other methods. Figure 11 compares the constraints from weak lensing with those from supernovae. The filled weak-lensing contours include tomography (with two redshift bins), the skewness, and the *COBE* normalization prior. The broad contours correspond to the current constraints from 42 supernovae (Perlmutter et al. 1999). The expected constraints derived from supernovae found in the *SNAP* deep survey are also shown. Note that these authors have marginalized over the time derivative w' of w and have thus not assumed that w was constant, as we have done. In addition, their constraints, unlike ours, include uncertainties due to systematics (see discussion in § 8). As before, all contours correspond to 68% confidence levels.

The *SNAP* weak-lensing survey will clearly greatly improve upon the current supernova constraints on w. It will also yield constraints that are comparable and somewhat orthogonal to those derived from the *SNAP* deep supernova survey. Note, however, that the *SNAP* weak-lensing survey is obtained from 5 months of observations rather than 32 months for the deep supernova survey.

The open contour in Figure 11 shows the effect of dropping the *COBE* prior for the weak-lensing constraints. The precision for Ω_m is hardly affected, but that for w is degraded by

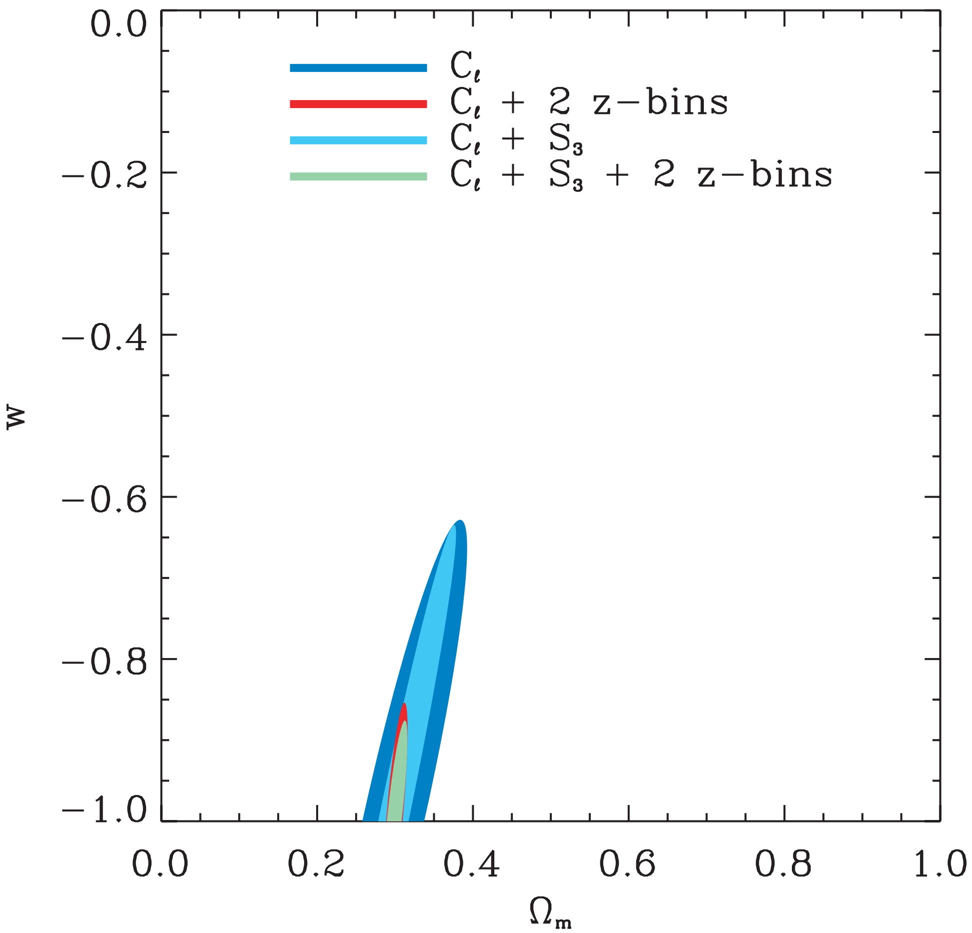

Fig. 10.—Constraints on Ω_m and w derived from combinations of the power spectrum without tomography (C_l), the power spectrum with two redshift bins, and the skewness S_3. Measurement of S_3 at the single scale $\theta = 2'$ is considered.

about 50%. Note that the above conclusions are contingent on the fact that lensing systematic uncertainties are subdominant. This will be discussed in the next section.

8. CONCLUSIONS

We have studied the capability of a wide-field space telescope to measure cosmological parameters with weak gravitational lensing. For this purpose, we have used the results of the image simulations described in Paper II to estimate the sensitivity to lensing shear for several survey strategies, using the *SNAP* mission as a concrete example. By combining the power spectrum measured in several redshift bins and the skewness of the convergence field, we find that the *SNAP* wide survey will provide measures of w and Ω_m with a 68% confidence level uncertainty of approximately 12% and 1.5%, respectively. These errors include marginalization over other parameters (h, A, n, and Ω_b) using *COBE* priors for the power spectrum normalization δ_h under the assumption of a flat universe, but they neglect systematics (see discussion below). These constraints are comparable and nearly orthogonal to those derived from supernovae in the *SNAP* deep survey. The constraints on w and Ω_m degrade by a factor of about 2 in the absence of tomography but are not affected very much if only the skewness is dropped.

We also studied how the constraints on these parameters depend on the survey strategy. We found that for a fixed observing time of 5 months, they improve slowly if the survey is made wider and shallower. This, combined with the limits imposed by the spacecraft telemetry, confirms the choice of the nominal parameters for the *SNAP* wide survey.

Note that our analysis relies on a number of assumptions. We first assumed that systematic errors are subdominant compared with statistical errors. The level of systematics will be greatly reduced for *SNAP*, as compared with ground-based surveys, thanks to the absence of atmospheric seeing and the stable thermal orbit of the spacecraft. This is confirmed by our assessment of the systematics for the *SNAP* design, described in Paper I. Further instrument and image simulations are however required to confirm these estimates. In addition, the *SNAP* optical and near-IR filter set will allow us to test and limit the impact of intrinsic galaxy alignments using photometric redshifts (see Heavens 2002 for a review).

We also assumed that the errors for the power spectrum and skewness are Gaussian and, thus, that the Fisher matrix provides good estimates of the errors. We also neglected potential cross talk between the power spectra in different redshift bins. While these effects are not expected to have a large influence on our error estimates (see White & Hu 2000), these approximations ought to be tested in the future using N-body simulations.

Another potential limitation arises from the theoretical uncertainties inherent in the computation of the matter power spectrum and bispectrum (see discussion in Huterer 2002; van Waerbeke et al. 2001a). Huterer indeed remarked that

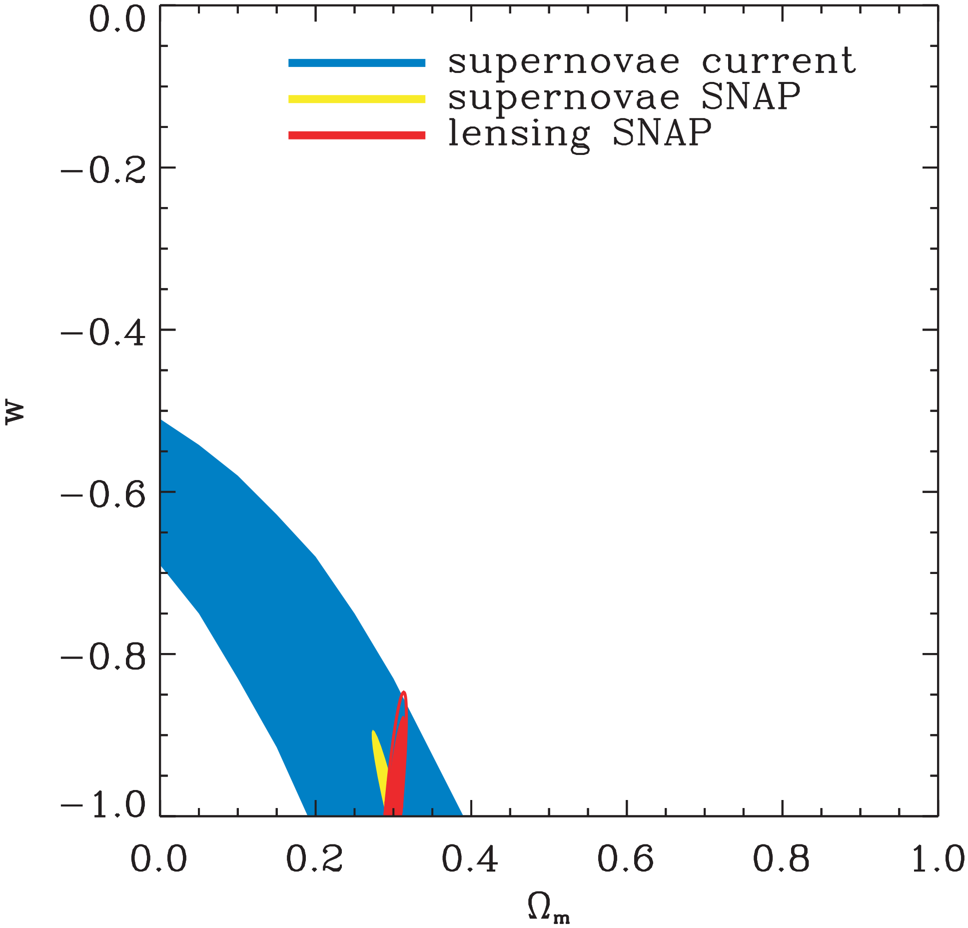

FIG. 11.—Comparison of the constraints derived from weak lensing and from supernovae. The current constraints from 42 supernovae (Perlmutter et al. 1999) are also displayed, along with those expected from the *SNAP* deep supernova survey. In the latter case, the time derivative w' of w was also marginalized over. The weak-lensing contours assume the use of two redshift bins for the power spectrum and use of the skewness. The filled and unfilled contours correspond to the constraints with and without the *COBE* normalization prior, respectively. As before, all contours correspond to 68% confidence levels.

significant differences exist between the different available formulae for the nonlinear corrections to the matter power spectrum (see, e.g., Peacock & Dodds 1996; Ma et al. 1999) in QCDM models. Larger and more accurate *N*-body simulations of QCDM models are needed to improve the accuracy of the fitting functions and to establish whether the finite accuracy of the theoretical predictions will be a limitation for the precision reached by future instruments.

Our work demonstrates that weak lensing is a powerful probe of both dark matter and dark energy. The complementarity of the constraints derived from weak lensing and supernovae validates the integration of both techniques in the science goals for *SNAP*. A joint analysis of the constraints that can be derived from weak lensing, supernovae, and cosmic microwave anisotropies on both w and its evolution is left to future work.

We thank Dragan Huterer for useful discussions and for sharing his results for comparison. We are grateful to Eric Linder for detailed comments on the manuscript and for fruitful discussions. The authors have also benefited from numerous discussions with the members of the *SNAP* collaboration. A. R. was supported in Cambridge by a PPARC Advanced Fellowship and by a Wolfson College Research Fellowship. The authors acknowledge the Sackler Fund in Cambridge for travel allowances.

REFERENCES

Bacon, D. J., Refregier, A. R., & Ellis, R. S. 2000, MNRAS, 318, 625
Bardeen, J. M., Bond, J. R., Kaiser, N., & Szalay, A. S. 1986, ApJ, 304, 15
Bartelmann, M., & Schneider, P. 2001, Phys. Rep., 4–5, 291
Benabed, K., & Bernardeau, F. 2001, Phys. Rev. D, 64, No. 083501
Bernardeau, F., van Waerbeke, L., & Mellier, Y. 1997, A&A, 322, 1
Bolzonella, M., Miralles, J.-M., & Pelló, R. 2000, A&A, 363, 476
Bunn, E. F., & White, M. 1997, ApJ, 480, 6
Cooray, A., & Hu, W. 2001, ApJ, 554, 56
Heavens, A. F. 2002, in The Shapes of Galaxies and Their Dark Halos, ed. P. Natarajan (River Edge, NJ: World Sci.), 21
Hoekstra, H., Yee, H. K. C., & Gladders, M. D. 2002, NewA Rev., 46, 767
Hu, W. 1999, ApJ, 522, L21
———. 2002, Phys. Rev. D, 66, No. 083515
Hu, W., & Keeton, C. R. 2002, Phys. Rev. D, 66, No. 063506
Hu, W., & Tegmark, M. 1999, ApJ, 514, L65
Hui, L. 1999, ApJ, 519, L9
Huterer, D. 2002, Phys. Rev. D, 65, No. 063001
Kaiser, N. 1998, ApJ, 498, 26
Ma, C.-P., Caldwell, R. R., Bode, P., & Wang, L. 1999, ApJ, 521, L1
Massey, R., et al. 2004, AJ, 127, 3089 (Paper II)
Mellier, Y., van Waerbeke, Bertin, E., Tereno, I., & Bernardeau, F. 2002, Proc. SPIE, 4847, 112

Munshi, D., & Wang, Y. 2003, ApJ, 583, 566
Peacock, J. A. 1997, MNRAS, 284, 885
Peacock, J. A., & Dodds, S. J. 1996, MNRAS, 280, L19
Perlmutter, S., et al. 1999, ApJ, 517, 565
Refregier, A. 2003, ARA&A, 41, 645
Rhodes, J., et al. 2004, Astropart. Phys., 20, 377 (Paper I)
Scoccimarro, R., & Frieman, J. A. 1999, ApJ, 520, 35
Spergel, D. N., et al. 2003, ApJS, 148, 175
Sugiyama, N. 1995, ApJS, 100, 281
Taylor, A. 2001, Phys. Rev. Lett., submitted (astro-ph/0111605)
van Waerbeke, L., Hamana, T., Scoccimarro, R., Colombi, S., & Bernardeau, F. 2001a, MNRAS, 322, 918
van Waerbeke, L., et al. 2001b, A&A, 374, 757
Weinberg, N. N., & Kamionkowski, M. 2003, MNRAS, 341, 251
White, M., & Hu, W. 2000, ApJ, 537, 1